Empirical relations for the sensitivities of solar-like oscillations to magnetic perturbations

René Kiefer ⬤★ and Anne-Marie Broomhall ⬤

Centre for Fusion, Space, and Astrophysics, Department of Physics, University of Warwick, Coventry CV4 7AL, UK

ABSTRACT

Oscillation mode frequencies of stars are typically treated as static for a given stellar model. However, in reality they can be perturbed by time-varying sources such as magnetic fields and flows. We calculate the sensitivities of radial p-mode oscillations of a set of models for masses between 0.7 and 3.0 $M_\odot$ from the main sequence to the early asymptotic giant branch. We fit these mode sensitivities with polynomials in fundamental stellar parameters for six stages of stellar evolution. We find that the best-fitting relations differ from those proposed in the literature and change between stages of stellar evolution. Together with a measure of the strength of the perturbation, e.g. of the level of magnetic activity, the presented relations can be used for assessing whether a star's observed oscillation frequencies are likely to be close to the unperturbed ground state or whether they should be adjusted.

Key words: asteroseismology – methods: numerical – stars: activity – stars: magnetic field.

1 INTRODUCTION

Owing to the revolution that the high-quality space-photometry data of *Kepler* (Borucki et al. 2010; Koch et al. 2010), CoRoT (Baglin et al. 2006; Auvergne et al. 2009), and *TESS* (Ricker et al. 2014) have brought about, many thousands of stars now have measured oscillation frequencies. These stars cover very different stages of evolution from the main sequence (e.g. Appourchaux et al. 2012; Lund et al. 2017) to subgiants (Appourchaux et al. 2012), red giants (e.g. Corsaro, De Ridder & García 2015; Kallinger 2019), core helium burning and asymptotic giant branch (AGB) stars (Kallinger 2019), and even white dwarfs (Hermes et al. 2017). Their oscillation frequencies can be subject to perturbations due to intrinsic time-varying sources, for example magnetic activity: it is well known that for the Sun, p-mode frequencies of low-degree modes at the frequency of maximum oscillation amplitude ν_{max} vary by about 0.4 µHz over the course of the solar activity cycle (Woodard & Noyes 1985; Elsworth et al. 1990; Libbrecht & Woodard 1990; Jiménez-Reyes et al. 1998). Similar behaviour has been observed for other main-sequence stars (e.g. García et al. 2010; Kiefer et al. 2017a; Santos et al. 2018).

Stellar activity appears to persist all the way through a star's evolution from the main sequence to the AGB: activity cycles have been detected on dozens of main-sequence stars (e.g. Baliunas et al. 1995); Aurière et al. (2015) measured magnetic fields at the surface of K and G giants; starspots have been detected on various types of stars (see references in Berdyugina 2005). Whether activity is generated by global cyclic dynamos or by local turbulent mechanisms is, in first approximation, not relevant for the perturbation of mode frequencies.

Several frameworks for understanding how various perturbations affect oscillation mode parameters have been developed, mostly with the Sun as the benchmark: Dziembowski & Goode (2004) used a variational approach to quantify the effect of the change of dynamical quantities over the solar cycle on mode frequencies. Coupling of normal modes within the framework of quasi-degenerate perturbation theory was investigated by Roth, Howe & Komm (2002) to calculate the effect of large-scale flows on p modes by Schad, Timmer & Roth (2013) to size the meridional circulation and by Kiefer, Schad & Roth (2017b) and Kiefer & Roth (2018) to assess the effect of global toroidal magnetic fields on p-mode frequencies and eigenfunctions. Hanasoge (2017) also exploits normal mode coupling, but with first-Born perturbation theory, to gauge the impact of Lorentz stresses on p-mode oscillations.

Recently, Howe et al. (2020) found that the solar ν_{max} varies by as much as 25 µHz over the Sun's activity cycle. In an asteroseismic context, it may thus be important to account for activity-related variations of ν_{max} and perturbations of measured mode frequencies when they are used to model the stellar structure or to infer global stellar parameters such as radius and mass (see also Kiefer, Broomhall & Ball 2019; Pérez Hernández et al. 2019). The magnitude of the frequency shifts can be estimated by the product of a factor accounting for the sensitivity of the oscillations to a perturbation and a factor for the strength of the perturbation, as we will detail in Section 3. In their effort to estimate the number of stars with detectable activity-related p-mode frequency shifts in *TESS* data, Kiefer et al. (2019) derived the mode sensitivity S to be proportional to $R M^{-1} \nu_{max}^{-1}$, where R is the stellar radius and M is stellar mass. This is very similar to the modal sensitivity contribution that Karoff et al. (2009) gave using the relation of Metcalfe et al. (2007), which was $S \propto R^{2.5} L^{0.25} M^{-2}$, where L is stellar luminosity. The scaling suggested by Chaplin et al. (2007) did not incorporate a factor for mode sensitivity but simply

★ E-mail: r.kiefer@warwick.ac.uk

Table 1. Initial masses and maximum time-steps between two models.

Initial mass ($M_\odot$)	Max. time-step (yr)
0.7, 0.8, 0.9, 1.0	$5 \cdot 10^8$
1.1, 1.2	$1 \cdot 10^8$
1.3, 1.5, 1.7	$5 \cdot 10^7$
1.8, 2.0, 2.2	$2 \cdot 10^7$
2.5, 2.8, 3.0	$1 \cdot 10^7$

assumes linear scaling of mode frequency shifts with the level of activity.

The exponents in these relations are fixed and it is thus expected that they cannot capture the variation of the mode sensitivity over the entire evolution from the main sequence to the early AGB. In this paper, we first describe the stellar evolutionary models we use to calculate the mode sensitivity in Section 2. The derivation of the mode sensitivity factor follows in Section 3. We then fit these sensitivities for six stages of stellar evolution with several polynomials in stellar fundamental parameters, as described in Section 4. The results are discussed in Section 5 and the conclusions we draw from these results follow in Section 6.

2 MODELS

We computed stellar models using Modules for Experiments in Stellar Astrophysics (MESA),[1] revision 12115 (Paxton et al. 2011, 2013, 2015, 2018, 2019), for 15 initial stellar masses and evolved them to the early AGB. We used the MESA test suite inlist for the evolution of a 1 $M_\odot$ star, which is stored in the MESA installation's folder '_\star\test_suite\1M_pre_ms_to_wd', adjusted the initial mass, and, in order to have a better resolution of the main-sequence and the core helium burning phases, the maximum time between two models. The initial masses and their respective maximum time-step values are given in Table 1. We terminated the evolution at the thermally pulsing (TP)-AGB, but as we are considering only stellar models with $\nu_{\max} > 1$ μHz (see Table 2), the more evolved models on the AGB are not included in our study. A sample MESA inlist is given in Appendix A1.

The models use the solar metal mixture of Grevesse & Sauval (1998) with a helium abundance of $Y_\odot = 0.248$ and a metallicity of $Z_\odot = 0.017$. The atmospheric model uses the MESA default, a standard Eddington grey atmosphere. The opacities are those of Iglesias & Rogers (1993), Iglesias & Rogers (1996), and the MESA option for C/O enhancement during and after helium burning is enabled with a base metallicity of 0.02.

The adiabatic radial p-mode eigenfunctions and eigenfrequencies of all models were computed with the oscillation code GYRE[2] (Townsend & Teitler 2013; Townsend, Goldstein & Zweibel 2018). A sample GYRE inlist is given in Appendix A2.

Fig. 1 shows a Hertzsprung–Russell diagram of the models we selected based on the requirements that they have a convection zone with a top boundary above 0.99 R, they have reached the main sequence, and their expected $\nu_{\max}$ is greater than 1 μHz . The requirement on the outer convection zone boundary ensures that p modes are detectable at the surface and are not suppressed by a thick outer radiative zone. We then separated the remaining models into six evolutionary stages based on the conditions listed in the second column of Table 2. The third column gives the final number of models

[1]http://mesa.sourceforge.net/
[2]https://bitbucket.org/rhdtownsend/gyre/

in each stage. The partitioning into main-sequence, subgiant and the red giant branch (RGB), core He burning, and AGB is founded on different stages of energy production and core composition. The subdivision of the RGB into lower RGB, upper RGB, and tip RGB models was guided by the phenomenology of the mode sensitivities. In particular, the separation of upper and tip RGB models improved the quality of the polynomial fits, as will be described in Section 4. Ten subgiant models are bluewards of the red edge of the instability strip defined by Chaplin et al. (2011) as

$$T_{\rm red} = 8907\,{\rm K} \cdot L^{-0.093},\tag{1}$$

where the luminosity L is in solar units. These models have square symbols in Fig. 1 and in all following plots.

3 MODE SENSITIVITY

We start with the variational expression for frequency shifts derived by Dziembowski & Goode (2004) (compare to their equation 18) and quoted by Metcalfe et al. (2007) in their equation 1:

$$\delta\nu_i = \frac{\int dV\,\mathcal{K}_i\mathcal{S}_i}{2I_i\nu_i},\tag{2}$$

where $\mathcal{K}_i$ is the kernel function relating perturbations caused by a source function $\mathcal{S}_i$ to the shifts $\delta\nu_i$, I_i is the mode inertia, and ν_i is the frequency of mode i in μHz. The integral is calculated over the entire stellar volume V. In the following, we will ignore the contribution of magnetic activity to equation (2) and assume that the resulting frequency shift is linear in the level of activity: $\delta\nu = S \cdot A$, where S is the sensitivity of a mode to a perturbation and A is a measure of the level of activity.

Just as in Metcalfe et al. (2007), we shall assume that the dominant term in the kernel of p modes is proportional to $|\text{div}\boldsymbol{\xi}|^2$, where $\boldsymbol{\xi}$ is the displacement eigenfunction. We consider only radial modes, which considerably simplifies the calculations. With this, the kernel function is

$$\mathcal{K} \propto \left| \frac{2}{r}\xi_r(r) + \frac{\partial\xi_r(r)}{\partial r} \right|^2,\tag{3}$$

where $\xi_r(r)$ is the radial displacement eigenfunction at radial position r.

We assume that the perturbation is located within one pressure scale height $H_{\rm p}$ below the photosphere with uniform and normalized strength

$$\mathcal{S} = \Theta(H_{\rm p} - d) = \begin{cases} 1, & \text{if } H_{\rm p} - d > 0 \\ 0, & \text{otherwise.} \end{cases}\tag{4}$$

Here, Θ is the Heaviside step function and d is the depth below the photospheric radius of the model. Thus, in this article we make no assumption about the level of magnetic activity affecting the modes or how this evolves over the stellar lifetime.

With this definition of the source function, we explicitly concentrate on (near-)surface magnetic activity affecting mode frequencies. From the Sun, it is known that the activity-related frequency shifts largely originate from the near-surface regions (e.g. Broomhall 2017). Similar behaviour has been observed on other solar-like oscillators by, e.g. Salabert et al. (2011, 2016a) and Kiefer et al. (2017a). Deeper located magnetic fields or core magnetic fields are likely to affect the temporal stability of mode frequencies less (e.g. Gough & Thompson 1990; Kiefer & Roth 2018). This is because such magnetic fields have a much smaller effect on p modes than near-surface fields due to the drop in sensitivity. Further, core fields are assumed to be stable over very long time-scales, meaning they

Table 2. Separation of evolutionary stages, number of models in each stage, relation in Table 3, which gives the lowest mean absolute error between fit and model sensitivities for each stage, and letter symbol that is used to identify this stage.

Stage	Conditions	# models	Best-fitting relation	ID
Main sequence	Centre hydrogen content $>10^{-5}$ $\nu_{max} > 1000$ µHz $T_{eff} < 7000$ K Contraction is finished $L_{tot} - L_H < 0.01$	383	5	A
Subgiants & lower RGB	Centre hydrogen content $<10^{-5}$ $\nu_{max} > 100$ µHz $T_{eff} < 7500$ K	230	5	B
Upper RGB	Centre hydrogen content $<10^{-5}$ 10 µHz $< \nu_{max} < 100$ µHz Helium core not ignited $L_{He} < 0.1 L_H$	257	3	C
Tip RGB	Centre hydrogen content $<10^{-5}$ 1 µHz $< \nu_{max} < 10$ µHz Helium core not ignited $L_{He} < 0.1 L_H$	382	6	D
Core He burning	Centre hydrogen content $<10^{-5}$ Centre helium content $>10^{-5}$ $\nu_{max} > 10$ µHz Helium burning $L_{He} > 0.1 L_H$	514	3	E
AGB	Centre hydrogen content $<10^{-5}$ Centre helium content $<10^{-5}$ $\nu_{max} > 1$ µHz	175	7	F
All	Top convection zone boundary $\geq 0.99\,R$	1941		

Note. L_{tot} is the total luminosity of the star including all sources. L_H and L_{He} are the contributions to the total luminosity from hydrogen and helium-burning processes, respectively.
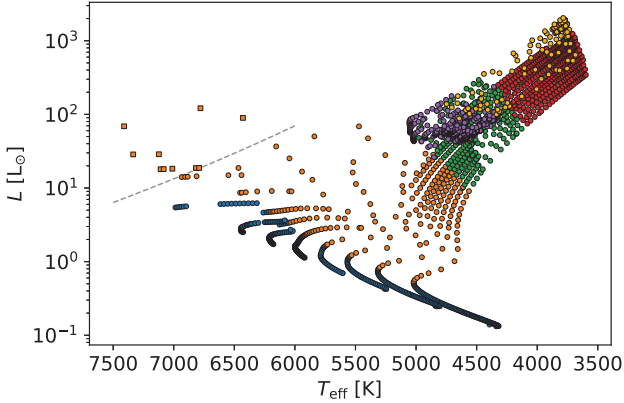
Figure 1. Hertzsprung–Russell diagram of the stellar models used in this study. Colours encode stellar evolutionary stages as defined in Table 2: main-sequence stars are blue, subgiants and lower red giant branch stars are orange, upper RGB models are green, tip RGB models are red, core helium burning models are purple, and AGB models are amber. The red edge of the instability strip is indicated by the dashed grey line.

are unlikely to bring about a mode frequency variation on observable time-scales. The deeper a magnetic field is located, the stronger it has to be to achieve the same level of frequency shift. We will discuss this further in Section 5.2.

In equation (2), the mode inertia I is calculated as

$$I = \int dV \rho |\boldsymbol{\xi}|^2, \qquad (5)$$

where the integral extends over the stellar volume V, ρ is density, and the displacement eigenfunction $\boldsymbol{\xi}$ can again be replaced by $\xi_r(r)$, as we consider only radial modes.

For simplicity, we investigate only the oscillation mode i closest to ν_{max}, which is calculated for each model with the scaling relation of Kjeldsen & Bedding (1995):

$$\nu_{max} = \nu_{max\odot} \cdot \left(\frac{M}{M_\odot}\right) \left(\frac{R}{R_\odot}\right)^{-2} \left(\frac{T_{eff}}{T_{eff\odot}}\right)^{-\frac{1}{2}}, \qquad (6)$$

with the calibrated solar reference value $\nu_{max\odot} = 3104$ µHz of Mosser et al. (2013), the solar values of mass $M_\odot = 1.9892 \cdot 10^{33}$ g, radius $R_\odot = 6.9598 \cdot 10^{10}$ cm, and effective temperature $T_{eff\odot} = 5777$ K as used in the MESA code. R and M are the model's photospheric radius and mass, respectively.

With the above definitions, equations (3), (4), and (5), and the stated assumptions, we calculate the right-hand side of equation (2) for the set of stellar models described in Section 2 and call this the mode sensitivity S of a star:

$$S = \frac{\int_{H_p}^{R} dV \, \mathcal{K}_{i,max}}{2 I_{i,max} \nu_{i,max}}, \qquad (7)$$

where the index 'i,max' indicates the mode closest to ν_{max}. The unit of S is cm g^{-1} µHz^{-1}.

To better illustrate how the observed behaviour of the mode sensitivities comes about, we show the three main quantities that make up the sensitivities, separately:
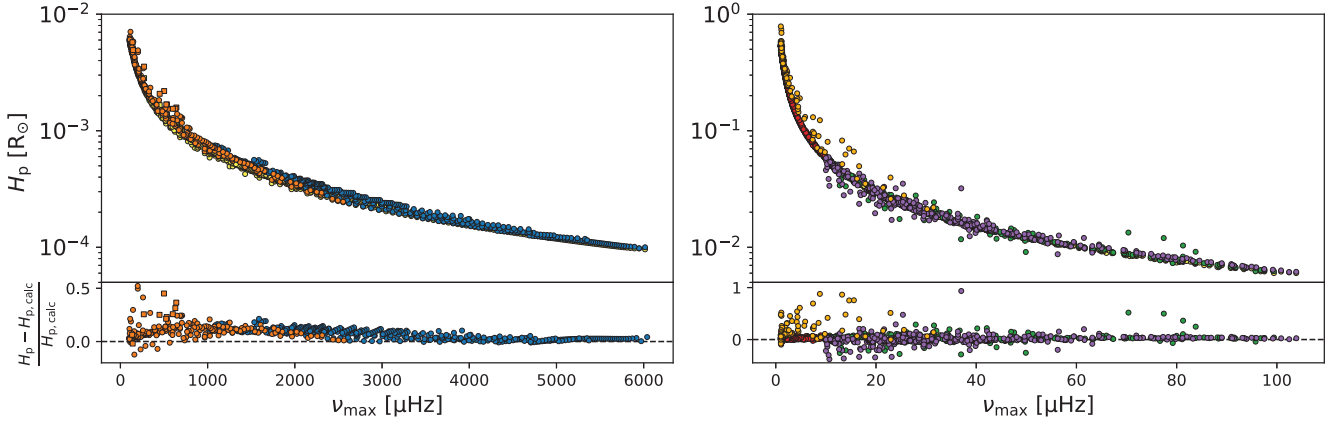
Figure 2. Pressure scale height H_p calculated from the MESA models as a function of ν_{max} for the six stages of stellar evolution as indicated in Table 2 with colours as in Fig. 1. Left-hand panel comprises the first two stages, right-hand panel the other four stages. Pressure scale heights calculated with equation (8) are shown in yellow but are largely covered by the models' data points. The bottom section of both panels shows the normalized difference between the calculated and the models' scale height.
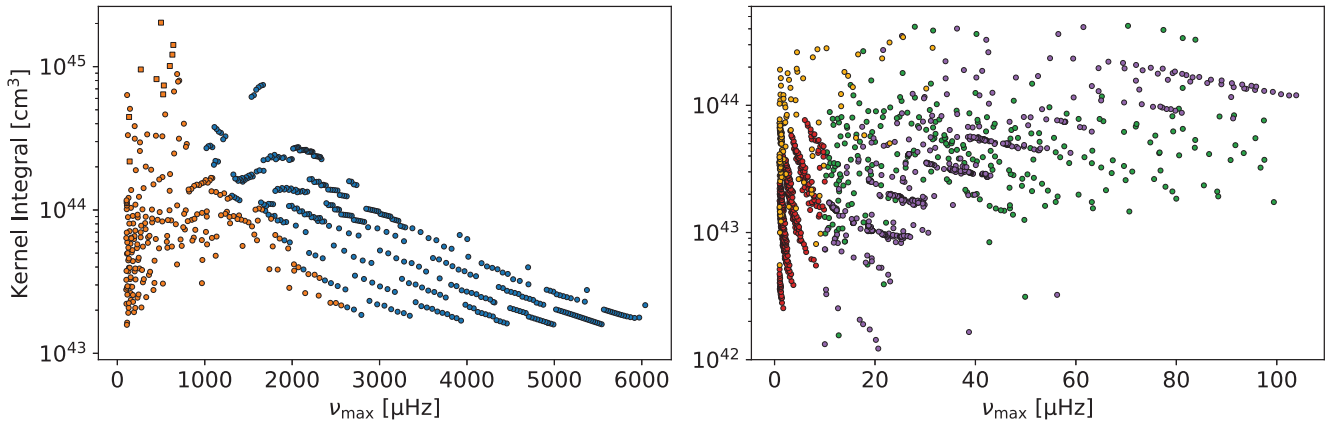
Figure 3. Numerator of equation (2) with model scale heights as shown in Fig. 2 over ν_{max} for the six stages of stellar evolution as indicated in Table 2 with colours as in Fig. 1. Left-hand panel comprises the first two stages, right-hand panel the other four stages.

3.1 Pressure scale height

The vertical distance over which hydrostatic pressure increases by a factor of e in a stratified atmosphere can be written as

$$H_p \propto \frac{P}{\rho g} \propto L^{0.25} R^{1.5} M^{-1}, \tag{8}$$

where it was taken that $\rho \propto MR^{-3}$ and $g \propto MR^{-2}$, where g is surface gravity. It was assumed that the stellar photosphere follows the equation of state of an ideal gas $P \propto \rho T$, where P is pressure and T is temperature. Further, the Stefan–Boltzmann law was used to express temperature as $T \propto L^{0.25} R^{-0.5}$.

Fig. 2 shows the pressure scale heights from the stellar models with the same colour code for the six stages of stellar evolution as described in Fig. 1 and detailed in Table 2. It is calculated for each model as the depth of that grid point at which the pressure is closest to $e \cdot P(\text{photosphere})$. The left-hand panel shows the first two stages and the right-hand panel comprises the last four stages in order to increase clarity as ν_{max} is the ordinate. The scale heights $H_{p, \text{calc}}$ calculated using equation (8) are shown in yellow data points. The values are scaled such that equation (8) yields a value of 150 km for the Sun.

As the models are in hydrostatic equilibrium, the models' pressure scale heights and the value obtained from equation (8) are within a

few per cent: the data points largely overlap. The bottom sections of the panels in Fig. 2 show the normalized difference between the two sets of values. The ideal gas assumption and that of a perfect blackbody will obviously affect the degree of accuracy of the rather simplistic equation (8) through stellar evolution where photospheric conditions highly vary. The largest relative systematic deviation between the models' scale heights and those from equation (8) is found during the subgiant stage. However, being within a few tens of per cent of the model values, equation (8) is a good approximation of stellar photospheric pressure scale heights.

3.2 Integral over kernel function

The integral extends over the stellar volume of the outer pressure scale height from the photospheric radius inwards. We assume the source function $\mathcal{S}$ to be unitless. As the unit of the eigenfunctions is cm, the unit of the numerator in equation (2) is cm^3.

The integral values of all investigated models are presented in Fig. 3 with colours and separation into two panels as in Fig. 2. On the main sequence, models around $\nu_{max} \approx 2000\,\mu\text{Hz}$ have the largest integral values. Higher mass stars have higher values than lower mass stars at same ν_{max}. For the subgiant and lower RGB stars, there is a spike in integral values for masses $1.5-2\,\text{M}_\odot$ around $\nu_{max} \approx$
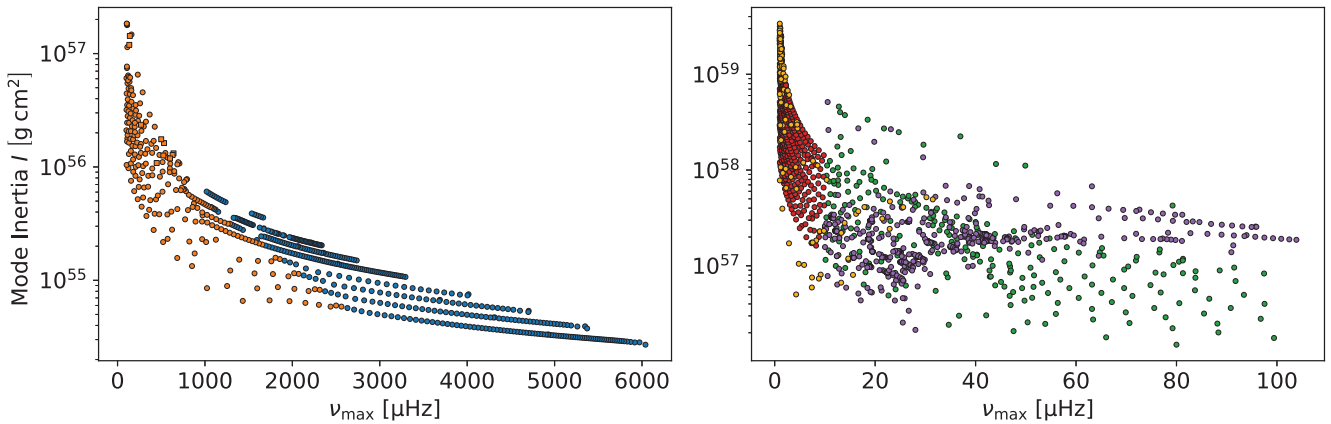
Figure 4. Same as Fig. 3 but for mode inertia as calculated by use of equation (5).

$600\,\mu\text{Hz}$. This increase is due to a surge in the pressure scale height for these stars; thus, more of the stellar radius and the kernel function are integrated over. The ridges correspond to different radial orders of the mode closest to ν_{max}. For the models in the tip RGB phase (red data points), the five ridges correspond to radial orders $n = 3$–7, counting from lowest to highest ν_{max}. To increase clarity of the figure, a few core He burning models with integral values $<10^{42}$ were cut.

3.3 Mode inertia

The integral in equation (5) extends over the entire stellar volume and amounts to a weighting of the stellar density with the eigenfunctions being the weights. Mode inertia is of the unit $\text{cm}^2\,\text{g}$. Fig. 4 shows the mode inertias with colours and separation into two panels as in Fig. 2. The ridges correspond to different mass values, with lower masses having smaller inertias. As the radial modes that are investigated here propagate throughout the star, mode inertias tend to be larger for higher mass stars. This also explains the steep increase with lower ν_{max}.

4 FITS OF POLYNOMIALS OF STELLAR PARAMETERS

The mode sensitivity value S of the mode eigenfunction closest to each model's estimated ν_{max} was calculated as described in Section 3. For the ease of plotting, S was multiplied by a factor of 10^{16} before the fits were carried out. Fig. 5 shows the values of S obtained as a function of ν_{max} for each evolutionary stage separately with letter labels in the top right of each panel as given for the different evolutionary stages in Table 2. Various polynomial models, which are described in the second column of Table 3, were then fitted to S independently for each evolutionary stage. The best-fitting parameters obtained from collecting 1000 least-squares fits, each with randomly chosen initial values for the parameters, are given in columns three to eight of Table 3. The initial values were limited to the half-open interval $[-50, 50)$. Fits for which the absolute of any exponent was >50 were neglected. The fits were repeated until 1000 stable samples were found. The best fit is chosen as that one with the smallest mean absolute error (MAE) between fit and calculated sensitivities. The last column of Table 3 gives the MAE of the best fit. The MAE is calculated as

$$\text{MAE} = \frac{\sum_{i=0}^{N} \left| S_{\text{model},i} - S_{\text{fit},i} \right|}{N - \text{dof}}, \qquad (9)$$

where, against the usual definition of the MAE, we subtract the number of degrees of freedom of each fit model, dof, from the number of data points N in order to penalize use of more free parameters.

The fit models were chosen such as to include global stellar parameters that are readily available either from asteroseismic analyses of space telescope light curves or from spectroscopic data. Thus, models 1 and 4 include only radius R, mass M, and frequency of maximum oscillation amplitude ν_{max}, which can be measured from sufficiently long photometric time series. Effective temperature T_{eff}, luminosity L, and surface gravity $\log g$, which enter models 2, 3, 5, 6, and 7 have to be obtained from, e.g. *Gaia* measurements or other spectroscopic observations of the star in question. Model 7 is a solely spectroscopic relation, should seismic parameters and estimates of mass and radius not be available.

Fig. 5 also shows the fits of relations to the models' sensitivity factors. Blue data points are sensitivities calculated from the MESA/GYRE models and amber circles show the best-fitting relation. Note that the ordinates of all panels are frequency of maximum oscillation amplitude ν_{max} with differing value domain between panels, as well as that the abscissae of all panels show the model mode sensitivities S with differing domains between panels. In the interest of improved clarity, the parameters of the best-fitting relation for each evolutionary group are given in Table 4.

5 DISCUSSION

The mode sensitivities for main-sequence stars (panel A of Fig. 5) are largely determined by the kernel functions. This is because their mode inertias do not change strongly through this stage for each stellar mass. The largest sensitivities are found for stars more massive than the Sun. This agrees with the findings of Santos et al. (2019), who found larger activity-related frequency shift values for stars of higher effective temperature. In Fig. 6, the main-sequence models' sensitivities are plotted as a function of effective temperature T_{eff}. The range of T_{eff} was limited to be the same as in panel (c) of fig. 3 of Santos et al. (2019) for easier comparison. The colour of the data points indicates stellar age, which, again, was capped at the same value as in Santos et al. (2019) at $13\,\text{Gyr}$. By comparison of these two figures, it can be seen that the mode sensitivities calculated here follow a very similar trend as the measured frequency shifts.

The bottom parts of the six panels in Fig. 5 show the normalized residuals between the models' sensitivities and the ones predicted by the best-fitting relations. For the main-sequence models, the residuals
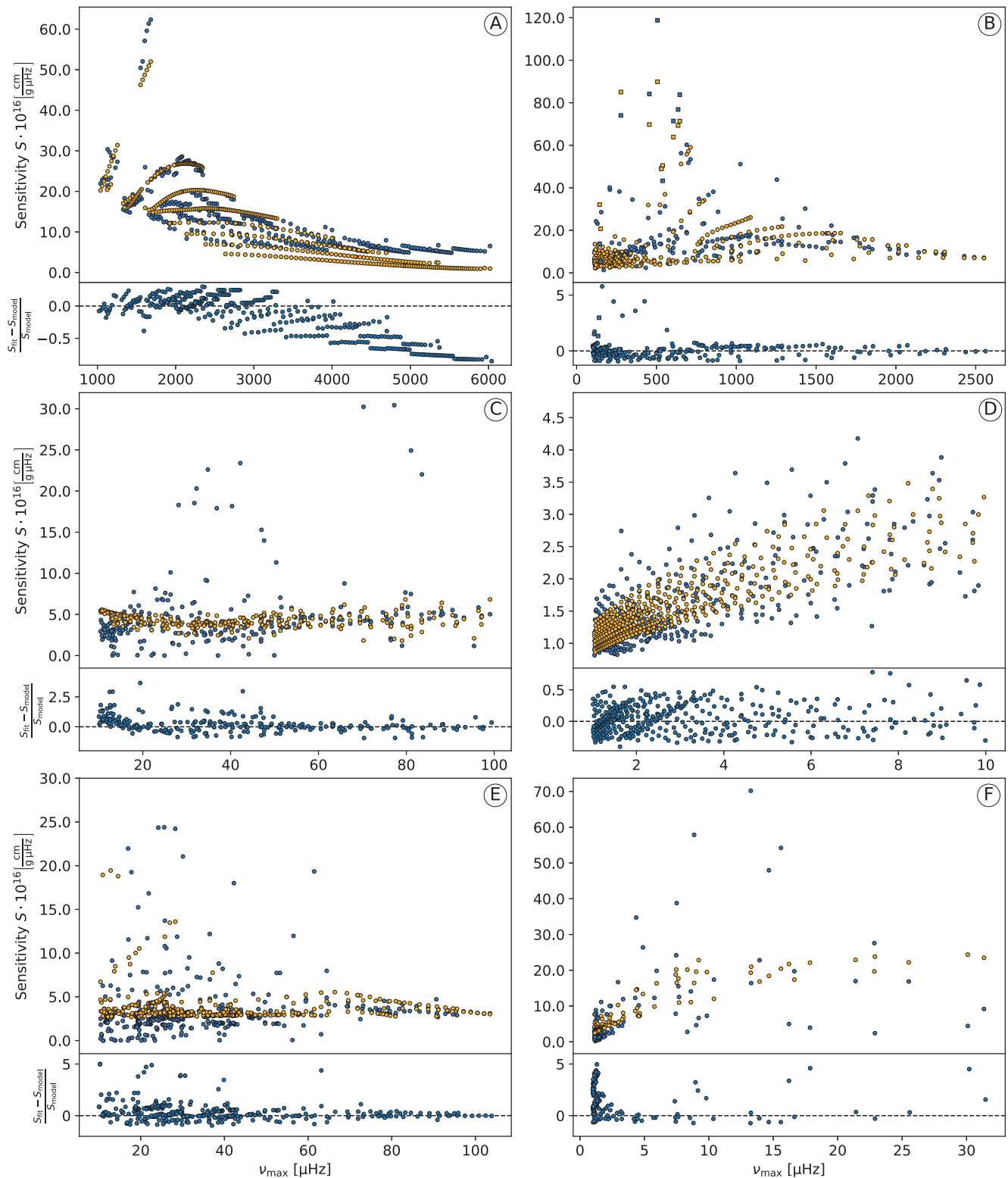
Figure 5. Fits of polynomials in fundamental stellar parameters to the calculated sensitivity factor *S*. Blue data points are model sensitivities and amber circles are the results of the best-fitting relation presented in Table 4. Panels show the six evolutionary stages as laid out in Table 2. Note that the ordinates and abscissae of the panels have differing value domains. The bottom section of each panel shows the normalized residuals between fitted and model sensitivities.

Table 3. Relations fitted to the theoretical mode sensitivities and their optimal parameters. Within each relation's paragraph, the six rows correspond to the six stages of evolution from Table 2 according to their letter symbol. The asterisks in the last column indicate the best model per evolutionary stage.

Number	Relation	Stage	α	β	γ	δ	ϵ	ζ	MAE	
1	$R^\alpha \cdot M^\beta$	A	-3.56	14.7					8.86	
		B	0.905	1.41					12.58	
		C	0.624	-0.512					2.55	
		D	0.138	-0.346					0.54	
		E	0.518	-0.483					2.26	
		F	-0.984	5.61					5.21	
2	$R^\alpha \cdot M^\beta \cdot T_{\rm eff}^\gamma$	A	-1.08	4.31	0.28				2.50	
		B	-4.79	8.71	0.471				8.22	
		C	-0.582	0.234	0.346				2.38	
		D	-0.847	-0.00659	0.439				0.31	
		E	-1.14	-0.189	0.503				2.31	
		F	-1.56	-0.564	0.923				4.03	
3	$R^\alpha \cdot M^\beta \cdot L^\delta$	A	-0.348	30.2		-4.64			8.31	
		B	-10.2	-9.83		7.13			10.43	
		C	14.6	3.11		-8.99			2.29	*
		D	-30.3	-7.34		19.6			0.36	
		E	-8.33	-1.51		5.42			1.96	*
		F	-11.2	-1.48		7.24			5.36	
4	$R^\alpha \cdot M^\beta \cdot \nu_{\rm max}^\epsilon$	A	-0.554	4.29			0.301		2.53	
		B	0.109	-0.198			0.319		8.25	
		C	0.109	-0.0856			0.369		2.38	
		D	0.023	-0.419			0.476		0.31	
		E	-4.92	-3.91			3.56		2.73	
		F	0.381	-0.757			0.807		4.30	
5	$R^\alpha \cdot M^\beta \cdot T_{\rm eff}^\gamma \cdot \nu_{\rm max}^\epsilon$	A	-13.4	5.5	6.61		-6.81		2.33	*
		B	-13.7	4.67	7.12		-7.36		6.34	*
		C	-13.0	6.26	6.53		-6.58		2.43	
		D	5.08	-2.82	-2.55		3.24		0.31	
		E	37.8	-25.5	-20.9		26.0		2.34	
		F	12.2	-6.76	-5.9		7.29		4.29	
6	$R^\alpha \cdot M^\beta \cdot L^\delta \cdot \nu_{\rm max}^\epsilon$	A	-4.23	-1.62		2.54	0.307		2.33	
		B	-3.82	-3.0		2.74	0.315		6.34	
		C	-37.3	-10.3		23.7	0.787		2.31	
		D	1.54	-0.0693		-0.98	0.495		0.31	*
		E	8.85	-2.93		-8.05	3.44		2.34	
		F	3.98	-0.406		-2.27	0.93		4.29	
7	$T_{\rm eff}^\gamma \cdot L^\delta \cdot \log g^\zeta$	A			-3.28	1.84		20.7	2.43	
		B			-3.18	1.79		20.4	7.62	
		C			0.00889	-0.00719		1.7	2.39	
		D			0.317	-0.383		0.433	0.31	
		E			0.603	-0.909		0.0101	2.36	
		F			0.549	-0.457		0.87	4.20	*

Table 4. Parameters of best-fitting relations per evolutionary stage.

Stage	R α	M β	$T_{\rm eff}$ γ	L δ	$\nu_{\rm max}$ ϵ	$\log g$ ζ
Main sequence	-13.4	5.5	6.61		-6.81	
Subgiants & lower RGB	-13.7	4.67	7.12		-7.36	
Upper RGB	14.6	3.11		-8.99		
Tip RGB	1.54	-0.0693		-0.98	0.495	
Core He burning	-8.33	-1.51		5.42		
AGB			0.549	-0.457		0.87
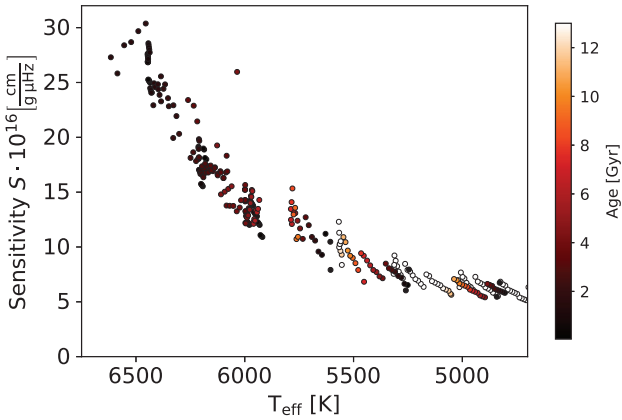
Figure 6. Mode sensitivities S of the main-sequence models as function of effective temperature T_{eff}. Colours show stellar age with capping of the colour bar at 13 Gyr.

are typically a few tens of per cent, with larger systematic residuals towards higher values of ν_{max}. Systematically overestimated sensitivities can also be found for models at the low ν_{max} end of panel C (upper RGB) and panel F (AGB). While the residuals can reach up to a factor of a few for some models, the overall agreement between the best-fitting relations' sensitivities and the model sensitivities is much better than for the sensitivity scaling relations from the literature, as we will detail later in this section. For purposes of presentation, we clipped the ordinate of the residuals' panels at 5 for stages B, E, and F. A few single outliers have normalized residuals > 5.

Subgiants (panel B of Fig. 5) have similar mode sensitivities to main-sequence stars. Isaacson & Fischer (2010) found that ≈ 10 per cent of subgiant stars show moderate to strong chromospheric activity. Thus, even though magnetic activity might not be widespread on this stage of stellar evolution, some stars can be expected to show significant activity-related frequency shifts. We also note that given, first, the findings of Balona (2019), who found evidence of starspots on hot stars, and, second, the large sensitivities of the few models in the instability strip, possible activity-related time variations of radial oscillation mode amplitudes and frequencies of, e.g. γ Dor, δ Scuti, and roAp variables might be worth further investigation. Amplitude as well as frequency variability has been detected on these types of variables by several groups including but not limited to Holdsworth et al. (2014), Breger (2016), and Bowman et al. (2016).

Overall, mode sensitivities decrease for upper (panel C) and tip RGB stars (panel D). However, given their low mode frequencies, even an activity cycle with solar-like amplitude can lead to detectable frequency shifts in such stars. This requires the cycle length to be of the order of the order of the observational baseline. For core helium burning stars (panel E), there are numerous models with sensitivities of the order of the main sequence again, in particular, at around $\nu_{max} \approx 30\,\mu$Hz. A few AGB models (panel F) have again rather large mode sensitivities. Depending on the strength and temporal scale of magnetic activity of upper RGB, core helium burning, and even early AGB stars, frequency shifts may be detectable for these types of stars in the available *Kepler* data set.

We do not give a physical interpretation to the best-fitting relation within each evolutionary group but provide them here as convenient shortcuts to estimate the mode sensitivity of individual stars based on a few readily accessible fundamental parameters. As can be seen from Table 3, the exponents in each model we fitted can differ quite

drastically from one evolutionary stage to the next. That being said, the jumps in the exponents for polynomials 2 and 4 are relatively small and should one be interested in using a single relation for all stars with only changing the exponents from stage to stage, then either one of these appears to be a justifiable choice.

It would in general be possible to obtain uncertainties for the exponents of the polynomial relations, e.g. by using a Markov-chain Monte Carlo estimation of the optimal exponents instead of the least-squares fit. However, the MAE of each fit reported in Table 3 can be used as a good estimation of the uncertainty if mode sensitivities are calculated.

To assess the impact of the number of models per evolutionary stage on the fits' results and quality, we redid the fits for two scenarios: first, we halved the number of models by taking every second model, effectively reducing the time resolution. With this, the polynomial relations per evolutionary stage that provide the best fit are the same as with the full model set. The exponents, however, do change, with the largest changes for the tip RGB and core helium burning stages. For these stages, the best-fitting relations are now $R^{6.79} \cdot M^{1.16} \cdot L^{-4.37} \cdot \nu_{max}^{0.60}$ and $R^{-3.81} \cdot M^{-0.54} \cdot L^{2.62}$, respectively. The residuals and the MAE are on a very similar level as with the full model set for all six stages.

In the second scenario, we lowered the number of models to 175 in each stage, which is the number of models of the AGB group. We chose these 175 models randomly from the full set. From this we find similar exponents for the best-fitting relations as for the full model set and the same relations that provide these best fits. The largest changes on the exponents occur again for the tip RGB models, for which the best-fitting polynomial is $R^{4.32} \cdot M^{0.53} \cdot L^{-2.77} \cdot \nu_{max}^{0.57}$ with a MAE of 0.30. For the core helium burning stage, the number of models is reduced by almost a factor of 3 (from 514 to 175). The best-fitting model now is $R^{-7.78} \cdot M^{-1.06} \cdot L^{5.04}$, which is quite similar to the one from the full model set. The removal of some of the higher sensitivity models in this stages leads to a somewhat smaller MAE of 1.52. Overall, the MAE of the fits and the residuals are very similar to the full model set.

From these two checks, we conclude that the best-fitting relations that we present in Table 4 provide reasonable estimates for the sensitivities in each evolutionary stage. The number of models within each evolutionary group and with it the temporal resolution that we chose for our grid of models appear adequate to capture the bulk behaviour of mode sensitivities.

In Fig. 7, the main-sequence (left-hand panel) and subgiant and lower RGB models' (right-hand panel) sensitivity factors of the best-fitting relation (amber data points) are compared to those calculated with the relations of Kiefer et al. (2019) (green) and Karoff et al. (2009) based on the derivations of Metcalfe et al. (2007) (red). As mentioned before, these two relations are rather similar – differing by a factor of merely $\propto \sqrt{T_{eff}}$ (see Kiefer et al. 2019) – thus, the green data points are largely covered by the red. We limit the comparison to these two evolutionary stages because these relations were not intended for use far off the main sequence. These two relations have fixed exponents and an unknown coefficient that gets lost in their derivation. As this coefficient has to be the same for all evolutionary stages, we obtained it by fitting the relations to the sensitivities of the main-sequence and subgiant and lower RGB models simultaneously. This gave a coefficient of 28525 for the Kiefer et al. (2019) relation and of 9.03 for the Karoff et al. (2009)–Metcalfe et al. (2007) relation. Their MAE to the combined data of both stages is 7.91 and 7.87, respectively. The combined MAE of the relations found here for these data is 4.28. For the main sequence individually, these values are 4.36 and 4.31 compared to 2.33 for
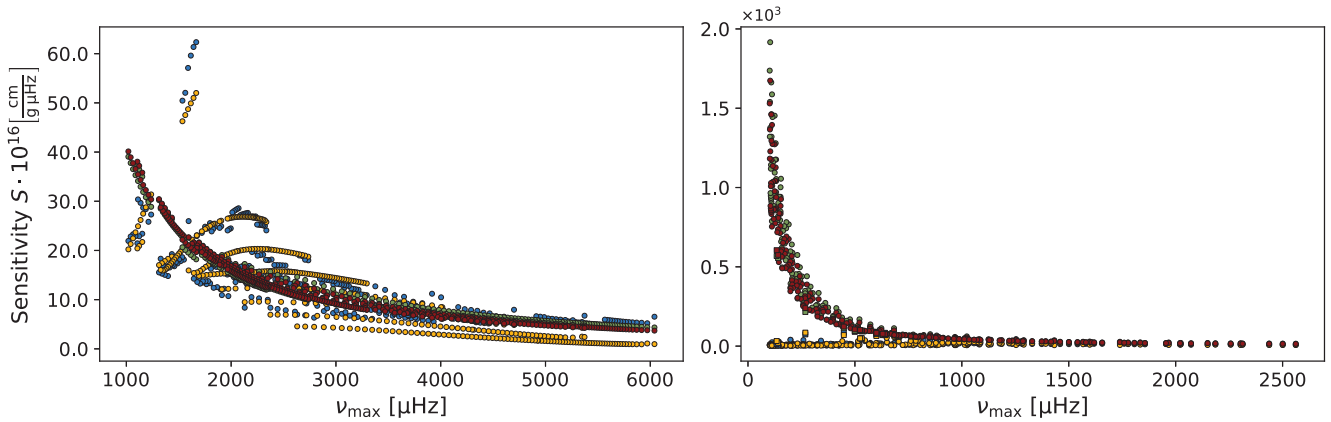
Figure 7. Comparison of fixed-exponent relations to the best-fitting relation. Blue data points are model sensitivities and amber circles are the results of the best-fitting relation found here. The relations of Kiefer et al. (2019) (green circles) and Karoff et al. (2009)–Metcalfe et al. (2007) (red circles) use the best-fitting multiplier based on the main-sequence models only. Left-hand panel is for main-sequence models, right-hand panel for subgiant and lower RGB models.

the relation found here. For the subgiants and lower RGB stage, they are 13.9 and 13.9 compared to 7.62 for the optimal relation. As can be seen, the relations from the literature do not reproduce the sensitivity factors as well as the empirical relations found here.

5.1 Application of the scaling relations

With the relations presented here and a measure of stellar activity, it is possible to estimate activity-related frequency shifts for stars from the main sequence to the AGB. We note that the prediction of frequency shifts has to be done with a normalization to a known activity level, typically with the Sun as the standard. For example, one would take the average logarithmic fraction of the solar luminosity that is emitted in the Calcium II H and K lines $\log R'_{HK\odot}$, multiply it by the sensitivity value obtained from the main-sequence relation, and scale the result to obtain the known solar cycle p-mode frequency shift amplitude of 0.4 μHz . This scaling factor can then be applied to stellar $\log R'_{HK}$ values and the sensitivities from the presented relations to give the expected full-cycle frequency shift values of the respective stars.

We use the main-sequence polynomial from Table 4 and known activity measures for the stars KIC 8006161 (HD 173701), KIC 10644235, and KIC 12009504 to predict their full-cycle frequency shifts. These stars' and the Sun's fundamental parameters as well as their $\log R'_{HK}$ and mean photometric activity $\langle S_{ph} \rangle$ are given in Table 5. See Mathur et al. (2014a, b) for the definition of $\langle S_{ph} \rangle$. The measured frequency shift amplitude $\delta\nu_{meas}$ was taken from Santos et al. (2018). It is simply calculated as the difference between their reported maximum and minimum value of the p-mode frequencies.

For KIC 8006161, we find that using $\log R'_{HK}$ to predict the full-cycle shift gives $\delta\nu_{pred,Ca} = 0.18 \pm 0.04\,\mu Hz$, whereas the measured shift is $\delta\nu_{meas} = 1.12 \pm 0.09\,\mu Hz$. Karoff et al. (2013) already found that this star shows an unexpectedly low-excess flux in the calcium lines. Thus, $\log R'_{HK}$ appears to be an unsuitable activity measure to predict the p-mode shift of this star in particular. For KIC 10644253, the predicted shift using $\log R'_{HK}$ is much closer to the observed value and the predicted and observed shifts are even in agreement, within the uncertainty, for KIC 12009504. It should be noted that the values of $\log R'_{HK}$ were not measured contemporaneously to the *Kepler* data. Depending on at what phase of a star's activity cycle $\log R'_{HK}$ is measured, it potentially underestimates the full-cycle shifts.

Using the mean photometric activity index $\langle S_{ph} \rangle$ to predict the frequency shifts, we find $\delta\nu_{pred,Sph} = 0.71 \pm 0.15\,\mu Hz$ for KIC 8006161, $0.91 \pm 0.24\,\mu Hz$ for KIC 10644253, and $0.37 \pm 0.11\,\mu Hz$ for KIC 12009504. These are in agreement with the measured values of KIC 10644253 and KIC 12009504. For KIC 8006161, this is again somewhat lower than the measured value. This can be due to two reasons: The sensitivity S is underestimated or $\langle S_{ph} \rangle$ is underestimated. As can be seen from the top left-hand panel in Fig. 5, our best relation underestimates the sensitivity by a few tens of per cent for stars with ν_{max} around 3500 μHz . Furthermore, KIC 8006161 has an inclination of 38^{+4}_{-3} degrees (Karoff et al. 2018). This can lead to an underestimation of its photometric activity, as active regions that lead to a global p-mode frequency shifts could hide on the out-of-sight portion of the star. Thus, it is likely that both factors contribute to the underestimation of this star's frequency shifts.

5.2 Assumption of a global near-surface perturbation

With equation (4), we located the cause of the frequency shifts entirely in the outer pressure scale height of the star with an isotropic distribution over the entire stellar sphere.

In a study of activity-related p-mode frequency shifts of *Kepler* stars, Salabert et al. (2018) found that for four stars of their 87 star sample, the shifts have an oscillatory behaviour as a function of mode frequency. Such a behaviour hints towards a cause of at least part of the frequency shifts, which is located deeper within the resonant p-mode cavity, possibly at the depth of the He II ionization zone. The sample of Salabert et al. (2018) is limited both in quality and size but poses the very intriguing question of where the (magnetic) perturbation that is associated with the observed frequency shifts is actually concentrated in the radial direction.

The frequency dependence of the shifts also depends on the spatial distribution of activity as was shown by, e.g. Kiefer & Roth (2018). Further, the spatial distribution of activity affects modes of different harmonic degree and azimuthal order differently (Moreno-Insertis & Solanki 2000). Analysing the frequency shifts of the radial and dipole modes of KIC 8006161 (HD 173701), Thomas et al. (2019) found that the active regions for this star are at higher latitudes than in the solar case and are distributed over a wider range.

We argue that any magnetic perturbation that is happening at a depth below the outer pressure scale height will eventually manifest in the near-surface layers. There, it will then lead to frequency shifts

Table 5. Fundamental parameters of test stars.

Star	R [$R_\odot$]	M [$M_\odot$]	$T_{\rm eff}$ [K]	$\nu_{\rm max}$ [μHz]	$\log R'_{\rm HK}$	$\langle S_{\rm ph} \rangle$ [ppm]	$\delta\nu_{\rm meas}$ [μHz]	$\delta\nu_{\rm pred,\,Ca}$ [μHz]	$\delta\nu_{\rm pred,\,Sph}$ [μHz]
Sun	1	1	5777	3104	-4.901	166.1 ± 2.6	0.4		
KIC 8006161	0.9293 ± 0.0083	0.9861 ± 0.0253	5488 ± 77	3574.7 ± 11.4	-5.03	492.4 ± 6.3	1.12 ± 0.09	0.18 ± 0.04	0.71 ± 0.15
KIC 10644253	1.1221 ± 0.0133	1.1748 ± 0.0385	6045 ± 77	2899.7 ± 22.8	-4.689	385.1 ± 8.9	1.07 ± 0.25	0.64 ± 0.17	0.91 ± 0.24
KIC 12009504	1.4120 ± 0.0193	1.1986 ± 0.0452	6179 ± 77	1865.6 ± 7.7	-4.949	131.2 ± 3.4	0.49 ± 0.16	0.42 ± 0.12	0.37 ± 0.11

Note. References. Radius and mass: Silva Aguirre et al. (2017). $T_{\rm eff}$ and $\nu_{\rm max}$: Lund et al. (2017) and references therein. $\log R'_{\rm HK}$: Santos et al. (2019), who used values from Karoff et al. (2013) and Salabert et al. (2016b). $\langle S_{\rm ph}\rangle$: Mathur et al. (2014b); except KIC 8006161: García et al. (2014). Measured frequency shift $\delta\nu_{\rm meas}$ from Santos et al. (2018). Solar values of $\log R'_{\rm HK}$ from Saar & Brandenburg (1999), $\langle S_{\rm ph}\rangle$ from Mathur et al. (2014b).

that are larger than those caused by deeper seated perturbations (Gough & Thompson 1990; Kiefer & Roth 2018). Further, we are not concerned with the frequency dependence of the frequency shifts here but focus on the full-cycle shift of the radial mode closest to $\nu_{\rm max}$. The assumption of the source function with equation (4) appears to be maintainable in this regard and certainly results in a very good estimate of the expected level of the mode sensitivities and thus of the frequency shifts. Still, given the results of Salabert et al. (2018) and Thomas et al. (2019), we again stress the importance of more detailed investigations of frequency shifts as a function of mode frequency and of harmonic degree if the data allow for such analyses.

6 CONCLUSIONS

We computed the sensitivity of p-mode oscillations to magnetic activity for a set of evolutionary stellar models. For this, we used a standard MESA inlist and adjusted only the initial mass (from 0.7 to 3.0 $M_\odot$) and maximum time-steps between models. We then used GYRE to compute p-mode eigenfunctions of all the models. The complete set of models was divided into six evolutionary stages. We found that modes are most sensitive to perturbations for main-sequence and subgiant stars. On the main sequence, sensitivity increases with higher mass. Lowest mode sensitivities are found for stars at the tip of the RGB.

In the calculation of the mode sensitivity S, we assumed that the leading terms in the kernel functions of p modes are proportional to div$\boldsymbol{\xi}$. We further assumed that the perturbations are concentrated within one pressure scale height below the photospheric radius of the models. Fits of polynomials in fundamental and widely available stellar parameters then gave relations for estimating these sensitivities.

In contrast to the relations for the mode sensitivity that have been used in the literature so far, when frequency shifts due to stellar activity were to be estimated, our relations are based on stellar models. The added flexibility of changing the exponents on the fundamental parameters in the polynomials between evolutionary stages certainly increases the capability of these relations to capture the true variation of the sensitivities through stellar evolution. The relation given by Karoff et al. (2009), which is based on derivations of Metcalfe et al. (2007), and the relation derived by Kiefer et al. (2019) are unable to reproduce the mode sensitivities of main-sequence stars and subgiant and lower RGB stars (which they were originally intended for) as well as the optimal relations presented here. In particular, the mass dependence of mode sensitivities and their change over time while the stars are on the main sequence is not well captured by these relations. For stars off the main sequence, these relations considerably overestimate mode sensitivities.

We used the optimal relation for the main sequence and tested it on three stars. We found that it is important to use activity

measures that are contemporaneous to the photometric data that are used to measure the p-modes whose shifts are to be predicted. If simple photometric activity indices are used, inclination of the stellar rotation axis can lead to an underestimation of the true level of activity and thus to underestimated shifts. Using the mean photometric activity index $\langle S_{\rm ph}\rangle$, we find overall solid agreement between the predicted and observed frequency shifts for the three stars that we investigated.

The derivation of the mode sensitivities is done only for purely radial oscillations, which ensures that the modes are pure p modes. This is of particular importance in RGB stars, where, e.g. dipole modes are often of mixed character, partly p mode and partly g mode. For non-radial modes, the calculation of the mode inertia and the kernel function would change, as the eigenfunctions include a horizontal part. It can be expected that mode sensitivities of mixed modes are weaker, as their mode inertia will have contributions from both the convective parts of the star (p mode) and the radiative part (g mode).

The reported relations and the presented mode sensitivities can also guide the selection of targets for future studies of activity-related p-mode frequency shifts: Mode sensitivities are largest for earlier main-sequence stars at around $\nu_{\rm max} = 2000\,\mu$Hz. Thus, in turn, frequency shifts can be expected to be largest for these stars. Further, subgiants in the range $400\,\mu$Hz $\lesssim \nu_{\rm max} \lesssim 800\,\mu$Hz show increased sensitivities and present good targets. Finally, we note that there appear several models with larger sensitivities in the upper RGB, core He burning, and the AGB stages. Such studies – optimally including oscillating stars at various evolutionary stages – could also aim at testing our relations, given known activity levels, fundamental stellar parameters, and p-mode frequency shifts.

The cardinal question driving all of this is: how do stellar dynamos operate and in what way do they change along stellar evolution? Simple time-resolved p-mode frequency measurements can play an important part in answering this.

DATA AVAILABILITY

The data sets underlying this article were generated with publicly available software and can be reproduced using the details provided in the appendix: MESA, http://mesa.sourceforge.net/, GYRE, https://bitbucket.org/rhdtownsend/gyre/

REFERENCES

Appourchaux T. et al., 2012, A&A, 543, A54
Aurière M. et al., 2015, A&A, 574, A90
Auvergne M. et al., 2009, A&A, 506, 411
Baglin A., Auvergne M., Barge P., Deleuil M., Catala C., Michel E., Weiss W., CoRoT Team, 2006, in Fridlund M., Baglin A., Lochard J., Conroy L., eds, ESA SP-1306: The CoRoT Mission Pre-Launch Status – Stellar Seismology and Planet Finding. Noordwijk, The Netherlands, p. 33
Baliunas S. L. et al., 1995, ApJ, 438, 269
Balona L. A., 2019, MNRAS, 490, 2112
Berdyugina S. V., 2005, Living Rev. Sol. Phys., 2, 8
Borucki W. J. et al., 2010, Science, 327, 977
Bowman D. M., Kurtz D. W., Breger M., Murphy S. J., Holdsworth D. L., 2016, MNRAS, 460, 1970
Breger M., 2016, A&A, 592, A97
Broomhall A. M., 2017, Sol. Phys., 292, 67
Chaplin W. J., Elsworth Y., Houdek G., New R., 2007, MNRAS, 377, 17
Chaplin W. J. et al., 2011, ApJ, 732, 54
Corsaro E., De Ridder J., García R. A., 2015, A&A, 579, A83
Dziembowski W. A., Goode P. R., 2004, ApJ, 600, 464
Elsworth Y., Howe R., Isaak G. R., McLeod C. P., New R., 1990, Nature, 345, 322
Farmer R., 2020, rjfarmer/mesaplot: Bug fixes, Available at: https://doi.org/10.5281/zenodo.3678482
García R. A., Mathur S., Salabert D., Ballot J., Régulo C., Metcalfe T. S., Baglin A., 2010, Science, 329, 1032
García R. A. et al., 2014, A&A, 572, A34
Gough D. O., Thompson M. J., 1990, MNRAS, 242, 25
Grevesse N., Sauval A., 1998, Space Sci. Rev., 85, 161
Hanasoge S. M., 2017, MNRAS, 470, 2780
Hermes J. J. et al., 2017, ApJS, 232, 23
Holdsworth D. L., Smalley B., Kurtz D. W., Southworth J., Cunha M. S., Clubb K. I., 2014, MNRAS, 443, 2049
Howe R. et al., 2020, MNRASL, 493, L49
Hunter J. D., 2007, Comput. Sci. Eng., 9, 90
Iglesias C. A., Rogers F. J., 1993, ApJ, 412, 752
Iglesias C. A., Rogers F. J., 1996, ApJ, 464, 943
Isaacson H., Fischer D., 2010, ApJ, 725, 875
Jiménez-Reyes S. J., Régulo C., Pallé P. L., Roca Cortes T., 1998, A&A, 329, 1119
Kallinger T., 2019, preprint (arXiv:1906.09428)
Karoff C., Metcalfe T. S., Chaplin W. J., Elsworth Y., Kjeldsen H., Arentoft T., Buzasi D., 2009, MNRAS, 399, 914
Karoff C. et al., 2013, MNRAS, 433, 3227
Karoff C. et al., 2018, ApJ, 852, 46
Kiefer R., Roth M., 2018, ApJ, 854, 74
Kiefer R., Schad A., Davies G., Roth M., 2017a, A&A, 598, A77
Kiefer R., Schad A., Roth M., 2017b, ApJ, 846, 162
Kiefer R., Broomhall A.-M., Ball W. H., 2019, Frontiers Astron. Space Sci., 6, 52
Kjeldsen H., Bedding T. R., 1995, A&A, 293, 87
Koch D. G. et al., 2010, ApJ, 713, L79
Lebigot E. O., 2019, Uncertainties: a Python package for calculations with uncertainties, Available at: http://pythonhosted.org/uncertainties/.
Libbrecht K. G., Woodard M. F., 1990, Nature, 345, 779
Lund M. N. et al., 2017, ApJ, 835, 172
Mathur S. et al., 2014a, J. Space Weather Space Clim., 4, A15
Mathur S., Salabert D., García R. A., Ceillier T., 2014b, A&A, 562, A124

Metcalfe T. S., Dziembowski W. A., Judge P. G., Snow M., 2007, MNRASL, 379, L16
Moreno-Insertis F., Solanki S. K., 2000, MNRAS, 313, 411
Mosser B. et al., 2013, A&A, 550, A126
Oliphant T. E., 2006, A guide to NumPy. Trelgol Publishing
Paxton B., Bildsten L., Dotter A., Herwig F., Lesaffre P., Timmes F., 2011, ApJS, 192, 3
Paxton B. et al., 2013, ApJS, 208, 4
Paxton B. et al., 2015, ApJS, 220, 15
Paxton B. et al., 2018, ApJS, 234, 34
Paxton B. et al., 2019, ApJS, 243, 10
Pérez Hernández F., García R. A., Mathur S., Santos A. R., Régulo C., 2019, Frontiers Astron. Space Sci., 6, 41
Reback J. et al., 2019, pandas-dev/pandas: v0.25.3, Available at: https://doi.org/10.5281/zenodo.3524604
Ricker G. R. et al., 2014, in Oschmann J. M., Jr, Clampin M., Fazio G. G., MacEwen H. A., eds, Space Telescopes and Instrumentation 2014: Optical, Infrared, and Millimeter Wave, Vol. 9143. International Society for Optics and Photonics, SPIE, p. 556
Roth M., Howe R., Komm R., 2002, A&A, 396, 243
Saar S. H., Brandenburg A., 1999, ApJ, 524, 295
Salabert D., Régulo C., Ballot J., García R. A., Mathur S., 2011, A&A, 530, A127
Salabert D. et al., 2016a, A&A, 589, A118
Salabert D. et al., 2016b, A&A, 596, A31
Salabert D., Régulo C., Hernández F. P., García R. A., 2018, A&A, 611, A84
Santos A. R. G. et al., 2018, ApJS, 237, 17
Santos A. R. G. et al., 2019, ApJ, 883, 65
Schad A., Timmer J., Roth M., 2013, ApJ, 778, L38
Silva Aguirre V. et al., 2017, ApJ, 835, 173
Thomas A. E. L. et al., 2019, MNRAS, 485, 3857
Townsend R., 2019, Mesa sdk for linux, Available at: https://doi.org/10.5281/zenodo.3560834
Townsend R. H. D., Teitler S. A., 2013, MNRAS, 435, 3406
Townsend R. H., Goldstein J., Zweibel E. G., 2018, MNRAS, 475, 879
Virtanen P. et al., 2020, Nature Methods, 17, 261
Waskom M. et al., 2018, mwaskom/seaborn: v0.9.0 (July 2018), Available at: https://doi.org/10.5281/zenodo.1313201
Woodard M. F., Noyes R. W., 1985, Nature, 318, 449

APPENDIX A: INLISTS

A1 MESA inlists

The following inlists were used to generate the set of stellar models with MESA. As described in Section 2, only the values for `initial_mass` and `max_years_for_timestep` were changed. As can be seen from these inlists, the maximal time between the calculated stellar models is 10 times smaller than those stated in Table 1, but we only saved every tenth model (`profile_interval = 10`). All keys that have the default MESA value are marked with a #, which should be removed before this inlist is used.

First, this inlist is used to evolve the star to the main sequence:

```
&star_job
    show_log_description_at_start   =  .false.
    create_pre_main_sequence_model  =  .true.
    save_model_when_terminate       =  .true.
    save_model_filename             =  'start.mod'
    required_termination_code_string =
        'max_model_number'
#    kappa_file_prefix               =  'gs98'
    pre_ms_relax_num_steps          =  50
    pgstar_flag                     =  .true.
/ ! end of star_job namelist
```

```
&controls
   max_years_for_timestep  =  5d7
   initial_mass  =  0.7

#    use_gold_tolerances  =  .true.
#    use_eosELM  =  .true.
#    use_eosDT2  =  .true.

   max_number_backups  =  1
   max_number_retries  =  5
   max_model_number  =  50

#    initial_z  =  0.02d0
   use_Type2_opacities  =  .true.
   Zbase  =  0.02d0

   varcontrol_target  =  1d-3

   photo_interval  =  50
   write_model_with_profile  =  .true.
   write_pulse_data_with_profile  =  .true.
   pulse_data_format  =  'GYRE'

   profile_interval  =  10
   model_data_prefix  =  'model'
   model_data_suffix  =  '.mod'
   max_num_profile_models  =  1500

   history_interval  =  10
   terminal_interval  =  10
   write_header_frequency  =  10
/ ! end of controls namelist
```

After this, the star is evolved until the end of the AGB with the following inlist:

```
&star_job
   show_log_description_at_start  =  .false.

   load_saved_model  =  .true.
   saved_model_name  =  'start.mod'
   save_model_when_terminate  =  .true.
   save_model_filename  =  'end_agb.mod'
   required_termination_code_string
        =  'envelope_mass_limit'

#    kappa_file_prefix  =  'gs98'

   change_initial_net  =  .true.
   new_net_name  =  'o18_and_ne22.net'

   new_surface_rotation_v  =  2 ! so-
lar (km sec^1)
   set_near_zams_surface_rotation_v_steps
=  10

   change_D_omega_flag  =  .true.
   new_D_omega_flag  =  .true.

   set_initial_cumulative_energy_error
=  .true.
   new_cumulative_energy_error  =  0d0
```

```
   set_initial_age  =  .true.
   initial_age  =  0

   set_initial_model_number  =  .true.
   initial_model_number  =  0

   pgstar_flag  =  .true.
/ ! end of star_job namelist

&controls
   max_years_for_timestep  =  5d7
   initial_mass  =  0.7

#    use_gold_tolerances  =  .true.
#    use_eosELM  =  .true.
#    use_eosDT2  =  .true.

   use_eps_mdot  =  .true.

   use_dedt_form_of_energy_eqn  =  .true.
   min_cell_energy_fraction_for_dedt_form
=  0
   use_eps_correction_for_KE_plus_PE_in_
dLdm_eqn
        =  .true.

   num_trace_history_values  =  2
   trace_history_value_name(1)  =
'rel_E_err'
   trace_history_value_name(2)
        =  'log_rel_run_E_err'

   max_number_backups  =  10
   max_number_retries  =  160
   max_model_number  =  6500
   backup_hold  =  3

#    initial_z  =  0.02d0

   use_Type2_opacities  =  .true.
   Zbase  =  0.02d0

   am_nu_visc_factor  =  0
   am_D_mix_factor  =  0.0333333333333333d0
#    D_DSI_factor  =  0
   D_SH_factor  =  1
   D_SSI_factor  =  1
   D_ES_factor  =  1
   D_GSF_factor  =  1
   D_ST_factor  =  1

   varcontrol_target  =  1d-3
   delta_lgL_He_limit  =  0.01d0

   envelope_mass_limit  =  1d-2 ! Msun

   cool_wind_full_on_T  =  9.99d9
   hot_wind_full_on_T  =  1d10
   cool_wind_RGB_scheme  =  'Reimers'
   cool_wind_AGB_scheme  =  'Blocker'
#    RGB_to_AGB_wind_switch  =  1d-4
   Reimers_scaling_factor  =  0.8d0
```

```
    Blocker_scaling_factor  =  0.7d0

    photo_interval  =  50
    write_model_with_profile  =  .true.
    write_pulse_data_with_profile  =  .true.
    pulse_data_format  =  'GYRE'
    profile_interval  =  10
    model_data_prefix  =  'model'
    model_data_suffix  =  '.mod'
    max_num_profile_models  =  1500
    history_interval  =  10
    terminal_interval  =  10
    write_header_frequency  =  10
 / ! end of controls namelist
```

A2 GYRE inlist

Name lists that were not used (e.g '&nad_output') are not listed here. The frequency interval to be scanned by GYRE, set by the freq_min and freq_max keys, is determined as $[\nu_{max} - 10 \cdot \Delta\nu, \nu_{max} + 10 \cdot \Delta\nu]$, with a minimum value for freq_min of $0.001\,\mu$Hz . Here, ν_{max} is calculated as described in Section 3 and the large frequency separation $\Delta\nu$ is calculated for each model via the scaling relation of Kjeldsen & Bedding (1995):

$$\Delta\nu = \Delta\nu_{\odot} \left(\frac{M}{M_{\odot}}\right)^{0.5} \left(\frac{R}{R_{\odot}}\right)^{-1.5}, \tag{A1}$$

with $\Delta\nu_{\odot} = 135\,\mu$Hz.

```
  &model
     model_type  =  'EVOL'
     file  =  'path_to_MESA_gyre_file'
     file_format  =  'MESA'
  /

  &mode
     l  =  0
  /

  &osc
     outer_bound  =  'JCD'
```

```
     inertia_norm  =  'RADIAL'
/

&num
   diff_scheme  =  'COLLOC_GL4'
/

&scan
   grid_type  =  'LINEAR'
   freq_min  =  freq_min_value
   freq_max  =  freq_max_value
   freq_min_units  =  'UHZ'
   freq_max_units  =  'UHZ'
   n_freq  =  500
/

&grid
   alpha_osc  =  20
   alpha_exp  =  4
   n_inner  =  10
/

&ad_output
   summary_file  =  'path_to_summary_file'
   summary_file_format  =  'TXT'
   summary_item_list  =  'M_star,R_star,
l,n_pg,
       freq,
freq_units,E,E_p,E_g,E_norm'
   mode_template  =  'path_of_output_file'
   mode_file_format  =  'TXT'
   mode_item_list  =  'l,n_pg,freq, freq_units,E,
   E_p,E_g,E_norm,x,xi_r,xi_h,rho,P'
   freq_units  =  'UHZ'
 /
```

This paper has been typeset from a T$_{\!E}$X/L$^{\!A}$T$_{\!E}$X file prepared by the author.